SIMULATION OF TIME-VARYING CORROSION RATE OF REBARS AND CORROSION-INDUCED CRACKS IN REINFORCED CONCRETE STRUCTURES SUBJECTED TO CHLORIDE CONTAMINATION

Bui Huy Tang[1], Tan Kang Hai[2]
[1]*Hanoi University of Civil Engineering,*
[1,2]*Nanyang Technological University*
Email: [1] buihuyta001@e.ntu.edu.sg, [2] CKHTAN@ntu.edu.sg
DOI: https://doi.org/10.59382/pro.intl.con-ibst.2023.ses1-26

ABSTRACTS: Corrosion of rebars and consequent corrosion-induced cracks significantly deteriorate durability and serviceability of reinforced concrete (RC) structures. This paper presents a time-dependent numerical model to simulate the entire corrosion process from initiation stage to crack propagation stage and consider the effect of cracks on the development of corrosion current density. Chloride transport model was implemented to determine evolution of corroded area in cross-section of rebars, while two configurations of corroded length along the bar axis was considered: (1) the entire length of rebar was simultaneously corroded and (2) the corroded length evolved gradually from the middle of the bar towards its two ends. Corrosion current density was calculated based on microcell and macrocell electrochemical mechanisms, while a mechanical model was established to simulate corrosion-induced concrete cracking. The results showed that the proposed numerical model was capable of predicting natural corrosion process and consequent crack propagation in RC structures subjected to chloride attack. When cracks developed through the concrete cover, corroded area spread faster, microcell and macrocell current densities increased, and the rust layer became more rounded.

KEYWORDS: Chloride attack, microcell corrosion, macrocell corrosion, corrosion-induced cracks, time-dependent.

1. INTRODUCTION

Reinforcement corrosion is considered as one of the main effects causing premature failure of reinforced concrete (RC) structures [1, 2]. Corrosion not only induces cracking and spalling of concrete cover but also decreases rebar diameter and bonding between the bar and concrete. Corrosion rate of rebars is the primary factor controlling structural deterioration process.

Over the last few years, several models have been proposed to simulate either penetration of corrosive substances into concrete [3, 4], electrochemical process of corroded rebars [5, 6] or corrosion-induced cracks [7, 8]. Only a few models incorporated all the three mechanisms to simulate the entire corrosion process [9, 10]. However, these models were established in 2D domain, thus, they could not incorporate macrocell corrosion in both circumferencial and longitudinal directions of rebars. In addition, most of them used uniform concrete cracking models to study nonuniform electrochemical corrosion, inducing incompatible between the two consecutive processes. Thus, it is critical to develop a 3D numerical model to simulate the entire nonuniform corrosion process from initiation stage to crack propagation stage and consider their mutual effects.

In the early 2000s, Kranc et al. proposed a numerical model based on finite element method to simulate macrocell corrosion of steel bars with the assumption of uniform rust formation around the rebar circumference [11]. Five years later, Isgor et al. employed 2D finite element analysis to determine corrosion rate of rebars [12]. However, they only simulated corrosion propagation without considering chloride transport in the initiation stage. In 2013, Cao et al. incorporated the effect of corrosion-induced cracks in simulating electrochemical process [13]. However, they applied an analytical thick-walled cylinder model with assumed uniform rust expansion to study crack propagation induced by nonuniform corrosion. Four years later, Zhu developed a chemical-mechanical model for both corrosion and subsequent cracks [10]. Although initiation and propagation stages were incorporated to investigate corrosion current density, the model was established in 2D cross-sectional domain with a single rebar. Thus, it could

not consider macrocell contribution from uncorroded bars in the longitudinal direction. In 2018, Cheng et al. implemented electrochemical theory to model nonuniform rust formation around the rebar's circumference which was subsequently used to study corrosion-induced concrete cracking [7]. However, they did not consider the effects of cracks on chloride penetration and corrosion rate. Last year, Qiu et al. introduced a numerical model to simulate crack evolution with time in concrete cover induced by rebar corrosion [14]. Although the model incorporated arbitrary distributions of aggregates and micropores in concrete, the effects of chloride transport and electrochemical process were not considered.

From the above literature review, it shows that although various models have been proposed in the last few decades, they only simulated individual processes either chloride transport, electrochemical kinetics or crack propagation. Only a few models studied the entire corrosion process from initiation stage to crack propagation stage. However, they did not consider the effects of corrosion-induced cracks on chloride penetration and electrochemical kinetics. In addition, most of the electrochemical models were established in 2D domain, thus, they could not incorporate macrocell corrosion from uncorroded rebars. Moreover, many cracking models simply assumed uniform rust distribution around the rebar based on some empirical functions without considering corrosion initiation process and electrochemical kinetics.

To overcome these research gaps, a 3D time-dependent numerical model is developed in this paper to simulate the entire corrosion process from initiation stage to crack propagation stage. Effects of cracks on corrosion initiation, microcell and macrocell current densities, as well as rust expansion, are investigated. The numerical model consists of three sub-models: (1) transport of chloride ions; (2) electrochemistry of corroded rebars and (3) mechanics of concrete cracking. Time-dependent evolution of corroded area around the rebar's perimeter is identified based on chloride content profile, while two configurations of corroded length along the rebar axis are simulated to study macrocell corrosion in 3D domain. In addition, rather than relying on empirical or analytical formulas of surface crack width evolution, a nonuniform FE model is developed to simulate nonuniform corrosion-induced concrete cracking.

2. SIMULATION OF CORROSION INITIATION AND PROPAGATION PROCESS

2.1. Corrosion initiation of rebars

Rebars embedded in concrete with high alkaline pore solution are protected from corrosion due to the formation of dense iron oxide film on the bar surface [1]. However, when chloride content at the rebar surface reaches a critical value, this protective film is breached and the rebar starts corroding [15, 16]. Transport of chloride in concrete is simulated based on Fick's second law using COMSOL Multiphysics V6.0 software as shown in Eq. (1).

$$\frac{\partial}{\partial x}\left(D_{cl,x}\frac{\partial C_{cl}}{\partial x}\right)+\frac{\partial}{\partial y}\left(D_{cl,y}\frac{\partial C_{cl}}{\partial y}\right)+\frac{\partial}{\partial z}\left(D_{cl,z}\frac{\partial C_{cl}}{\partial z}\right)=\frac{\partial C_{cl}}{\partial t} \quad (1)$$

where $D_{cl,x}$, $D_{cl,y}$ and $D_{cl,z}$ are the respective chloride diffusion coefficients in x, y and z directions; C_{cl} is the chloride content.

Time-dependent evolution of corroded area in circumferential direction is modelled by dividing the cross-section of rebar into 36 elements as shown in Figure 1a. When chloride content at the surface of these elements attains the critical value, they are considered as corroded part, while the other elements remain uncorroded (Figure 1b). Two configurations of corroded length along the rebar's axis are simulated to investigate the effect of localised corrosion in 3D domain on microcell and macrocell current densities. In the first configuration, the entire length of rebar is corroded at the same time, while the corroded length evolves progressively from the middle of the bar towards its two ends as corrosion develops in the second configuration.

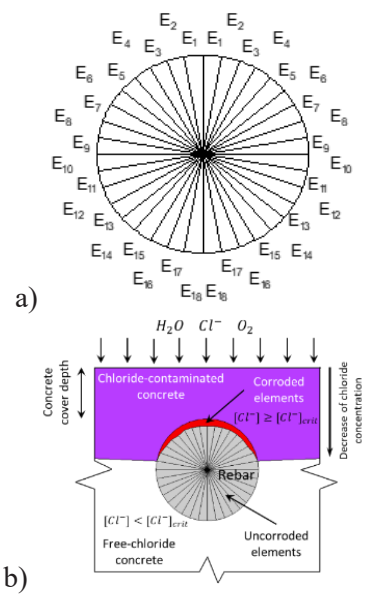

Figure 1. Simulation of corroded area: a) Devision of rebar cross-section; b) Corroded area in circumferential direction

2.2. Microcell and macrocell corrosion

After corroded rebar is identified, microcell and macrocell mechanisms are employed to determine total corrosion rate. In corroded rebars, both iron oxidation (Eq. (2)) and oxygen reduction reactions (Eq. (3)) happen, while only the latter (Eq. (3)) occurs in uncorroded rebars. When both reactions take place in the same region or close to each other, corrosion is termed as "*microcell*". Conversely, it is named "*macrocell*" when anodic reaction happens in corroded rebar, while cathodic reaction occurs in uncorroded bar. As a result, concrete resistivity significantly affects macrocell corrosion, while it has negiligible effect on microcell corrosion.

$$Fe \rightarrow Fe^{2+} + 2e^- \quad (2)$$

$$O_2 + 2H_2O + 4e^- \rightarrow 4OH^- \quad (3)$$

Relationships between overpotential and current density of anodic and cathodic reactions on corroded rebars are respectively shown in Eq. (4) and Eq.(5), while Eq. (6) shows the relationship for cathodic reaction on uncorroded rebars [9, 13].

$$\phi_{a,act} = \phi^0_{a,act} + \beta_{a,act} log\left(\frac{i_{a,act}}{i^0_{a,act}}\right) \quad (4)$$

$$\phi_{c,act} = \phi^0_{c,act} + \beta_{c,act} log\left(\frac{i_{c,act}}{i^0_{c,act}} \times \frac{C^s_{O_2}}{C_{O_2}}\right) \quad (5)$$

$$\phi_{c,pas} = \phi^0_{c,pas} + \beta_{c,pas} log\left(\frac{i_{c,pas}}{i^0_{c,pas}} \times \frac{C^s_{O_2}}{C_{O_2}}\right) \quad (6)$$

where $\phi_{a,act}$, $\phi_{c,act}$ and $\phi_{c,pas}$ are the respective overpotentials of anodic, cathodic reactions on corroded rebars and cathodic reaction on uncorroded rebars; $\phi^0_{a,act}$, $\phi^0_{c,act}$ and $\phi^0_{c,pas}$ are the respective equilibrium potentials of anodic, cathodic reactions on corroded rebars and cathodic reaction on uncorroded rebars; $\beta_{a,act}$, $\beta_{c,act}$ and $\phi_{c,pas}$ are the respective Tafel slopes of anodic, cathodic reactions on corroded rebars and cathodic reaction on uncorroded rebars; $i_{a,act}$, $i_{c,act}$ and $i_{c,pas}$ are the respective current densities of anodic, cathodic reactions on corroded rebars and cathodic reaction on uncorroded rebars; $i^0_{a,act}$, $i^0_{c,act}$ and $i^0_{c,pas}$ are the respective anodic, cathodic exchange current densities on corroded rebars and cathodic exchange current density on uncorroded rebars; $C^S_{O_2}$ is the oxygen concentration on concrete surface; C_{O_2} is the oxygen concentration inside concrete which is calculated based on Fick's second law as follows [13]:

$$\frac{\partial}{\partial x}\left(D_{O_2,x}\frac{\partial C_{O_2}}{\partial x}\right) + \frac{\partial}{\partial y}\left(D_{O_2,y}\frac{\partial C_{O_2}}{\partial y}\right) + \frac{\partial}{\partial z}\left(D_{O_2,z}\frac{\partial C_{O_2}}{\partial z}\right) = \frac{\partial C_{O_2}}{\partial t} \quad (7)$$

where $D_{O2,x}$, $D_{O2,y}$ and $D_{O2,z}$ are the respective oxygen diffusion coefficients in x, y and z directions. Their magnitude is calculated as in Eq. (8) [17]:

$$D_{O_2(x,y,z)} = 2.183 \times 10^{-9} \times \left(\frac{w}{c}\right)^{2.346} \times T^{0.423} \times H^{-3.247} \quad (8)$$

where *w/c* is the water-to-cement ratio; *T* is the temperature of concrete; *H* is the relative humidity.

When only microcell corrosion at corroded rebars is considered, microcell current density and potential are determined based on the following boundary conditions [18]:

$$i_{mic,act} = i_{a,act} = i_{c,act} \quad (9)$$

$$\phi_{mic,act} = \phi_{a,act} = \phi_{c,act} \quad (10)$$

where $i_{mic,act}$ and $\phi_{mic,act}$ are the respective microcell current density and corrosion potential.

On the other hand, macrocell current density is determined based on potential gradient between the anodic reaction at corroded rebar and the cathodic reaction at uncorroded rebar. Potential distribution in concrete is obtained by solving Laplace's equation as shown in Eq. (11) which satisfies nonlinear boundary conditions in Eqs. (12), (13) and (14).

$$\frac{\partial^2 \phi}{\partial x^2} + \frac{\partial^2 \phi}{\partial y^2} + \frac{\partial^2 \phi}{\partial z^2} = 0 \quad (11)$$

$$\phi = \phi_{mic,act} \text{ on } \Gamma_{act} \quad (12)$$

$$\phi = \phi_{mic,pas} \text{ on } \Gamma_{pas} \quad (13)$$

$$\frac{\partial \phi}{\partial n_1} = 0 \text{ on } \Gamma_{sf} \quad (14)$$

where Γ_{act} is the surface of corroded rebars; Γ_{pas} is the surface of uncorroded rebars; Γ_{sf} is the free concrete surface; n_1 is the direction vector normal to concrete surface.

When potential distribution at corroded and uncorroded rebars is determined, macrocell current density is calculated based on Ohm's law as follows:

$$i_{mac,act} = -\frac{1}{R_c}\frac{\partial \phi}{\partial n_2} \quad (15)$$

where R_c is the concrete resistivity between corroded and uncorroded rebars; n_2 is the direction vector normal to equipotential contours.

Total corrosion current density at the corroded rebar is calculated based on both microcell and macrocell corrosion as follows:

$$i_{a,act}=i_{mic,act}+i_{mac,act} \quad (16)$$

The numerical model of corrosion process is developed using COMSOL Multiphysics V6.0 software with input electrochemical parameters adopted from previous publications as shown in Table 1 [10-12, 19].

Table 1. Input electrochemical parameters

Parameters	Value	Unit
$\beta_{a,act}$	60	mV/decade
$\beta_{c,act}$ and $\beta_{c,pas}$	-160	mV/decade
i_a^0	180×10^{-6}	A/m^2
i_c^0	6×10^{-6}	A/m^2
ϕ_a^0	-780	mV
ϕ_c^0	160	mV
D_{cl}	6×10^{-12}	m^2/s

Corroded depth around the rebar is calculated based on total corrosion current density using Faraday's law as follows [20]:

$$d_{corr}(E_i,t)=\frac{1}{\rho_s}\frac{M}{n_{Fe}F}\int_{t_1}^{t_2} i(E_i,t)dt \quad (17)$$

where E_i is the element i of the rebar; $d_{corr}(E_i,t)$ is the corroded depth at element E_i and time t; M is the atomic mass of iron; ρ_s is the density of steel; t_1 is the time when E_i starts corroding; t_2 is the time of calculation; $i(E_i,t)$ is the corrosion current density at element E_i and time t.

3. SIMULATION OF NONUNIFORM CORROSION-INDUCED CRACKS

Once corroded depth around the rebar is identified, free rust expansion is calculated by multiplying the corroded depth with the expansion coefficient. It was reported that akaganeite (β-FeOOH) with expansion coefficient of 3.5 is the most expansive corrosion product detected in reinforced concrete. This value is adopted in this simulation for conservative purposes. Thickness of free rust layer is calculated as follows:

$$d_{free}(E_i,t)=(\alpha_{exp}-1)\times d_{corr}(E_i,t)-t_{pr} \quad (18)$$

where α_{exp} is the expansion coefficient of rust; t_{pr} is the thickness of porous zone around the rebar where rust fills in first before exerting expansive pressure onto surrounding concrete. Its magnitude of 15 μm is used for subsequent simulation as adopted in previous publications [8, 21].

To simulate rust expansion, thermal analogy method is employed incorporating both mechanical properties of rust and confinement effects of concrete and steel. The cross-section of rebar is divided into 36 elements and different temperature gradients are imposed on different rebar's angular elements to model nonuniform expansion of the rust layer as shown in Figure 2. Magnitude of temperature gradient at element E_i and time is calculated as in Eq (19).

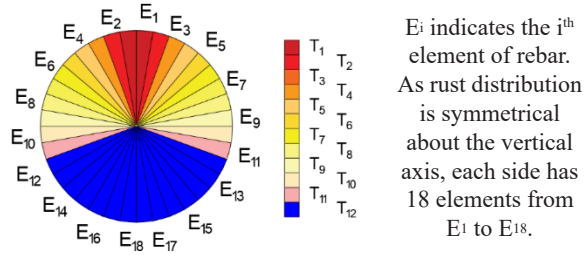

Figure 2. Modelling rust expansion by thermal analogy method

$$\Delta T(E_i,t)=\frac{d_{free}(E_i,t)}{2\times\alpha_L\times R_s} \quad (19)$$

where α_L is the linear thermal expansion coefficient (11.75×10^{-6} m/mK); R_s is the radius of rebar.

Mechanical properties of rust such as elastic modulus and Poisson's ratio are applied to the rust layer between the rebar and concrete. It should be noted that these two parameters are dependent on various factors such as types of steel, conditions of steel-concrete interface and corrosive environments. Their magnitude can be varied in a wide range. Thus, for simulation of a particular RC structure, elastic modulus of rust and Poisson's ratio should be obtained from experiments. In this study, since the verified specimens were placed in a splash zone near the sea with rich chloride ions, rust was expected to be more porous and softer than steel. Therefore, values of 500 MPa and 0.3 are adopted from published studies for the respective rust elastic modulus and Poisson's ratio [22, 23].

Crack propagation in RC structures is modelled using Abaqus/CAE 2017 software. Damaged plasticity model is implemented to simulate nonlinear behaviour of concrete, while rebar and rust are considered as elastic materials. Elastic-plastic damage constitutive relationship in concrete is expressed as follows:

$$\sigma=(1-d)D_{0,e}:(\varepsilon-\varepsilon_p)=D_e:(\varepsilon-\varepsilon_p) \quad (20)$$

where σ is the compressive/tensile stress in concrete; ε and ε_p are respectively the compressive/tensile strains and plastic strains; $D_{0,e}$ and D_e are respectively the initial compressive/tensile elastic

stiffness and degraded elastic stiffness of concrete; d is the compressive/tensile damage factor, representing the degradation of concrete stiffness after cracking which is calculated as follows:

$$d=1-\sqrt{\frac{\sigma}{E_0\varepsilon}} \quad (21)$$

where E_0 is the elastic stiffness of concrete.

In the FE cracking model, 4-node bilinear quadrilateral elements are employed for concrete, while 3-node linear triangle elements are for steel bars and rust layers. As a result, plastic strain is used to indicate crack patterns, while surface crack width is determined by multiplying residual tensile strain of concrete after cracking with th size of cracked elements as shown below [7, 10]:

$$w_{cr}=\left(\varepsilon_t-\frac{f_t}{E_0}\right)H \quad (22)$$

where w_{cr} is the crack width; ε_t is the total strain; f_t is the tensile strength of concrete; E_0 is Young's modulus; H is the cracked element size.

4. EFFECTS OF CRACKS ON TRANSPORT OF CHLORIDE AND OXYGEN

When corrosion becomes severe and vertical cracks propagate through the concrete cover, penetration of chloride and oxygen in concrete is accelerated, thereby affecting corrosion kinetics of rebars. When chloride ions penetrate faster into concrete, not only the rebar is corroded earlier but the spread of corroded area also increases, leading to changes in cathode/anode ratio and corrosion rate. Furthermore, the presence of more oxygen on the rebar surface expedites cathodic reaction which subsequently increases corrosion rate. Transport of chloride ions in cracked concrete is simulated based on an analytical model developed by Jang et al. as shown in Eq. (23) [24]:

$$\frac{D_{cl}^{cr}}{D_{cl}}=1+\frac{\left(w_{cr}-w_{cr}^{crit}\right)\times\beta_{cr}}{L_{con}}\times\frac{D_0^{cr}}{D_{cl}} \quad (23)$$

where D_{cl}^{cr} and D_{cl} are respectively the diffusion coefficients of chloride ions in cracked and uncracked concretes; D_0^{cr} is the diffusion coefficient of chloride in free solution (2.03×10^{-9} m^2/s); w_{cr}^{crit} is the critical crack width, below this value diffusion of chloride is not affected by cracks; β_{cr} is the crack geometry factor accounting for the influence of connectivity and tortuosity of cracks; L_{con} is the length of interested region of concrete.

On the other hand, oxygen penetration in cracked concrete is calculated based on that in uncracked concrete through an empirical equation as follows [25]:

$$D_{O_2}^{cr}=\begin{cases}D_{O_2} & \text{if } w_{cr}<w_{cr}^{th}\\ D_{O_2}\times\left(\frac{w_{cr}}{w_{cr}^{th}}\right)^3 & \text{if } w_{cr}\geq w_{cr}^{th}\end{cases} \quad (24)$$

where $D_{O_2}^{cr}$ is the diffusion coefficient of oxygen in cracked concrete; w_{cr}^{th} is the threshold value of crack width where cracks do not have any physical effect on oxygen penetration.

Surface crack width obtained from the FE model is used to investigate the effects of nonuniform corrosion-induced cracks on microcell and macrocell current densities. Once crack length reaches the rebar, effects of cracks on corrosion initiation and propagation are considered.

5. EXPERIMENTS FOR PARTIAL VALIDATION OF NUMERICAL MODELS

Experiments conducted by Valipour et al. are used to partially validate the proposed numerical model in terms of chloride penetration, microcell and macrocell current densities [26]. Corrosion-induced concrete cracking was simulated based on validated FE method as presented in the previous publications [7, 8]. In this experimental programme, RC specimens with dimensions of 550 mm × 300 mm × 200 mm were cast using Portland cement II as shown in Figure 3.

Nine rebars with a diameter of 14 mm were installed, in which three rebars were placed on the top, while six rebars were positioned at the bottom. The top rebars had a concrete cover depth of 30 mm, while it was 156 mm for the bottom rebars. Side and bottom surfaces of the specimens were sealed to prevent penetration of chloride and oxygen. As a result, only the top three rebars were corroded, while the bottom rebars were not corroded. The specimens were placed in splash zone near the sea in Qeshm Island for 650 days to simulate marine environmental effects [26, 27]. To quantify microcell

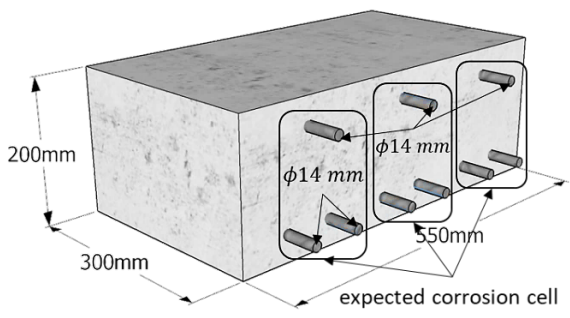

Figure 3. RC samples for validating microcell and macrocell current densities [26]

corrosion at top corroded rebars, galvanostatic pulse technique was employed, while macrocell current was measured between the top corroded rebar and the corresponding bottom uncorroded bars by using ammeter instrument following ASTM G109-99a.

In addition, three 150 mm-concrete cubes were prepared to test compressive strength at 28 days. Its magnitude was 34.2. MPa. Tensile strength of 3.2. MPa and Young's modulus of 27.5 GPa were calculated from the compressive strength based on ACI 318-14 [28].

To determine profile of chloride content in concrete, prism samples with dimensions of were cast with the same mix design as shown in Figure 4 [27]. After curing, the prisms were exposed to the marine environment in Qeshm Island for 9 months. Then, concrete cores were extracted to quantify chloride content at three positions along the cover depth (e.g., 1 mm, 20 mm and 30 mm) (Figure 4).

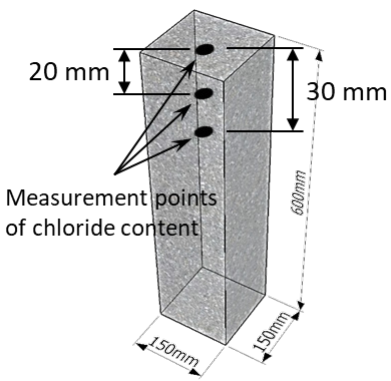

Figure 4. Concrete prism for validating chloride penetration [26, 27]

6. RESULTS AND DISCUSSIONS

6.1. Time-dependent development of corroded area

To determine evolution of corroded area with time, chloride content along the concrete cover needs to be identified. Chloride profiles obtained from the proposed models with and without considering corrosion-induced cracks against the test results after 9 months of exposure are shown in Figure 5. It can be seen that the presence of through cracks hastens chloride penetration. Chloride transport rate from the concrete surface to a depth of 20 mm is greater when vertical cracks are considered, while they are similar between the cracked and uncracked models at locations deeper than 20 mm. This is because after 9 months of exposure, cracks only propagate to a depth of 20 mm. In addition, the difference in chloride profiles between the two models after 9 months is not so significant as the vertical crack width at this time is small (0.10 mm obtained from the numerical simulation). Most importantly, it shows that the diffusion model gives good agreement with the test results. Thus, it can be used for subsequent electrochemical studies.

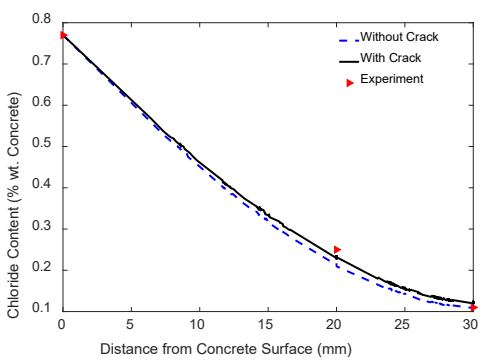

Figure 5. Chloride profiles after 9 months exposure

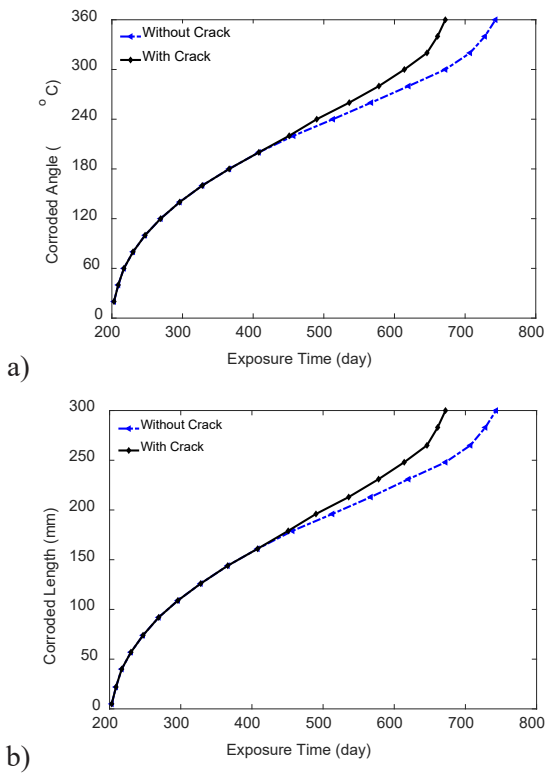

Figure 6. Evolution of corroded area: a) Circumferential direction; b) Longitudinal direction with varying corroded length

Based on the chloride profiles, evolutions of corroded area in circumferential and longitudinal directions with varying corroded length are respectively shown in Figure 6a and b. It can be seen that the presence of cracks shortens the time needed to cause the same corroded area as in the uncracked model.

6.2. Microcell and macrocell current densities

After corroded area of rebars is determined from the chloride profiles, microcell and macrocell mechanisms are employed to calculate corrosion rate. Figure 7a shows time-dependent

development of total corrosion current density for two configurations of corroded length, while the effect of corrosion-induced cracks is presented in Figure 7b. It can be seen from Figure 7a that at the beginning, the constant corroded length model gives slightly better agreement with the test results than the varying corroded length model. However, after around 15 months of exposure, the constant corroded length model deviates away from the test results, while the varying corroded length model is in good agreement. This is because after this period, cracks develop through the concrete cover, expediting the penetration of oxygen and chloride towards the rebars. It leads to the increase of corrosion rate. The results infer that the numerical model with localised nonuniform corrosion in both circumferential and longitudinal directions in 3D domain provides better prediction of corrosion current density than the model with constant corroded length.

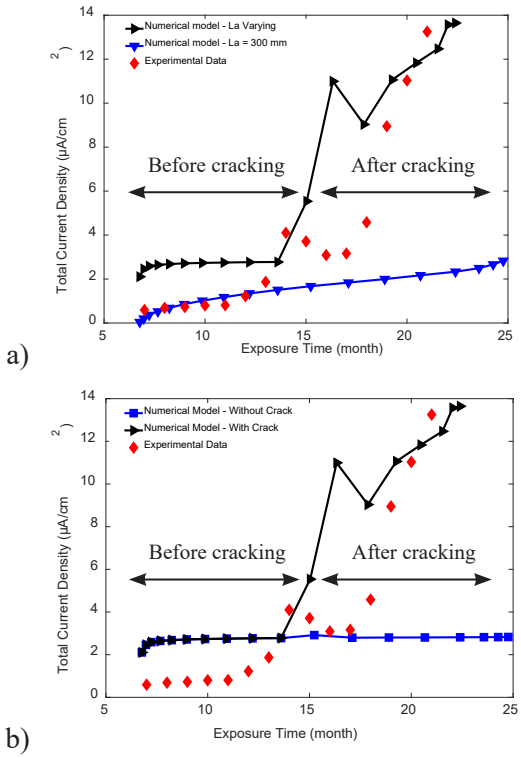

Figure 7. Corrosion current density with time: a)Varying corroded length vs. constant corroded length; b) With and without incorporating cracks

Figure 7b shows the effect of corrosion-induced cracks on corrosion rate of rebars. The model incorporating cracks gives better agreement with the test results than the model without cracks. In the beginning, when crack length has not reached the rebar, the two models provide the same results. However, as the crack develops through the concrete cover, corrosion current density substantially increases in the cracked model, which agrees well with the test results. Conversely, in the uncracked model, corrosion current density does not increase. It should be noted that as cracks propagate through the concrete cover, total current density does not increase continually but decreases after around 16 months and then increases again (Figure 7). This is because the spread of rust over the upper part of the rebar's surface to the lower part and the formation of lateral cracks induce compressive stress in concrete blocks above the middle bar, thereby reducing concrete surface crack width and decreasing corrosion current density. After reaching equilibirum, as corrosion becomes more severe, crack width continues increasing, resulting in a rise of corrosion rate. The difference of current density between the model and the experiment when the exposure time was from around 14 months to 18 months might be due to the assumption of constant crack width and straight crack direction along the concrete cover in the model.

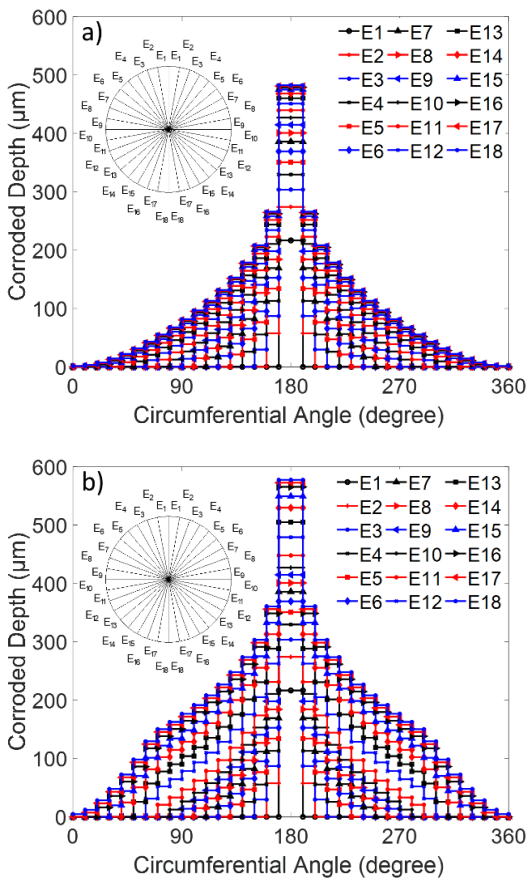

Figure 8. Nonuniform distribution of corroded depth at different times: a) Model without cracks; b) Model with cracks

Once the corrosion current density is identified, corroded depth around the rebar's circumference is calculated using Faraday's equation. Nonuniform distributions of corroded depth simulated by the uncracked and cracked models at different times

are shown respectively in Figure 8a and b. It can be seen that when cracks are incorporated into the model, the corroded depth is greater and the shape of corroded area is more rounded compared to the model without cracks.

Contributions of microcell and macrocell current densities obtained from the cracked model with localised corrosion in 3D domain are shown respectively in Figure 9a and b. It shows that the proposed model has good agreement with the test results for both microcell and macrocell corrosion. In this particular experiment, macrocell contribution from bottom uncorroded rebars is less significant than microcell corrosion at the corroded bar itself. This might be because concrete resistance between the bottom and top rebars is large as they are located at more than 10 times the rebar's diameter, diminishing ionic current between them. It can also be seen from Figure 9 that after cracks develop through the concrete cover, microcell and macrocell current densities increase by 5 to 6 times compared to that when cracks have not reached the rebars.

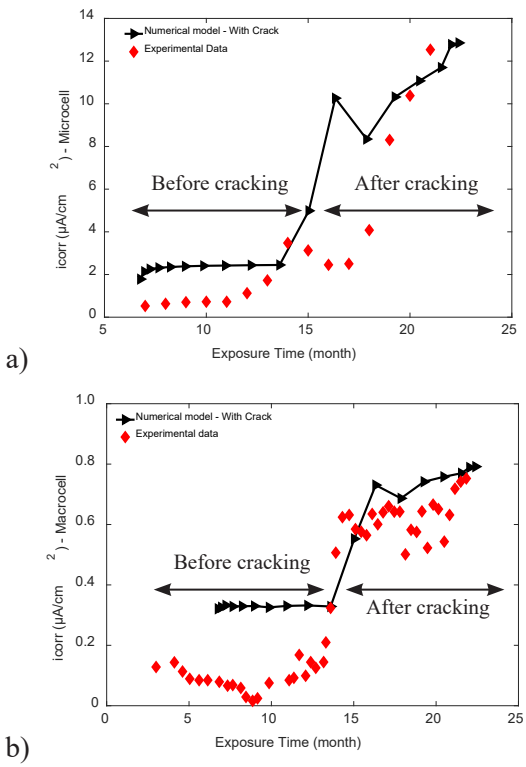

Figure 9. Corrosion current density: a) Microcell corrosion; b) Macrocell corrosion

6.3. Crack propagation in concrete induced by corrosion

Time-dependent evolution of crack patterns induced by corrosion is shown in Figure 10. As corrosion develops, two lateral cracks initially evolve from the rebar to the two sides. At the same time, a vertical crack propagates from the concrete surface inwards towards the rebar. The vertical crack above the middle rebar is less severe than those above the left and the right bars. This is because rust expansion and crack formation from the side rebars decrease tensile stress in concrete block above the middle bar. When corrosion becomes severe, not only do the three existing cracks lengthen, but another crack also occurs at the bottom of the rebars and develops into the concrete body. Once the vertical cracks propagate through the concrete cover, penetration of chloride and oxygen from the atmosphere is facilitated, thereby expediting corrosion process and increasing both microcell and macrocell current densities. The results of corrosion-induced cracks are incorporated into the transport and electrochemical models to investigate their effects on corrosion rate of rebars as presented in Figure 6, Figure 7 and Figure 8.

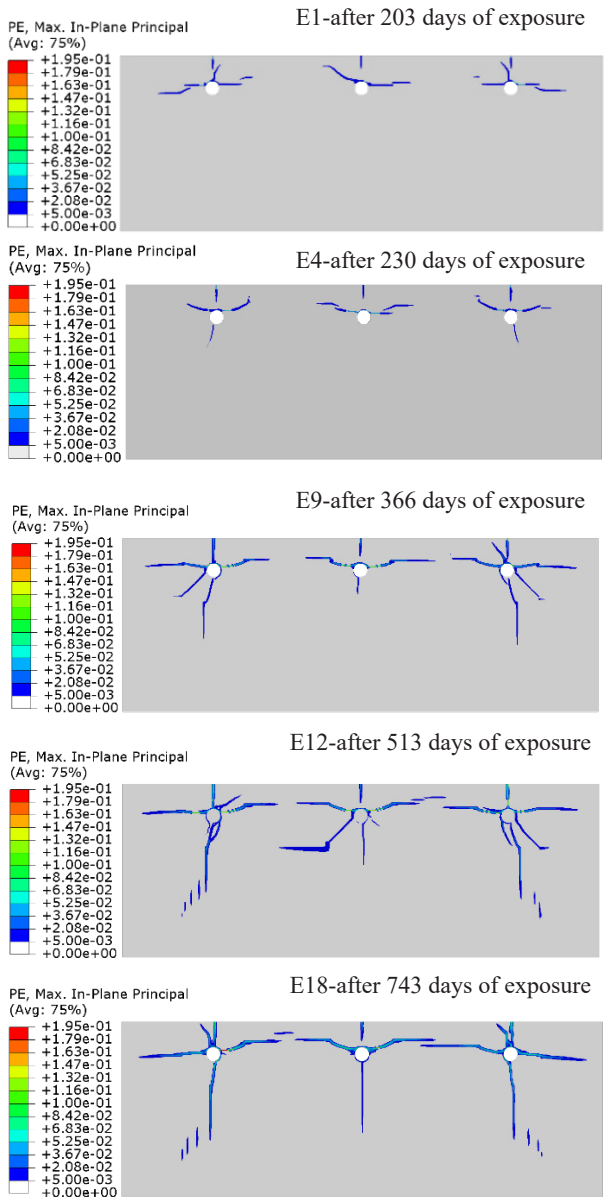

Figure 10. Crack propagation with time induced by corrosion

7. CONCLUSION

A time-dependent nonuniform numerical model is developed in this study to simulate the entire corrosion process and consequent corrosion-induced cracks in RC structures. The numerical model consists of three sub-models including transport model of corrosive substances, electrochemical model of rebar corrosion and numerical model of concrete cracking. From the study, various conclusions are drawn as follows:

The proposed model is capable of simulating natural corrosion process and consequent cracking in RC structures subjected to chloride contamination. The employment of both microcell and macrocell mechanisms, as well as time-varying corroded area in 3D domain enables the model to simulate actual localised corrosion phenomena in RC structures.

When corrosion-induced cracks are incorporated into the numerical model, corroded area evolves faster, microcell and macrocell current densities increases and the shape of rust layer is more rounded.

For RC specimens with three top corroded rebars and six bottom uncorroded rebars and they are located far away with more than ten times the bar diameter, macrocell contribution from the uncorroded rebars is less significant compared to microcell corrosion on the corroded rebar itself.

REFERENCE

[1] L. Bertolini, B. Elsener, P. Pedeferri, E. Redaelli, R. Polder, *Corrosion of steel in concrete,* Wiley Online Library 2013.

[2] S. Ahmad, *Reinforcement corrosion in concrete structures, its monitoring and service life prediction - a review,* Cement and concrete composites 25(4-5) (2003) 459-471.

[3] B. Martın-Pérez, S.J. Pantazopoulou, M. Thomas, *Numerical solution of mass transport equations in concrete structures,* Computers & Structures 79(13) (2001) 1251-1264.

[4] Y. Li, X. Chen, L. Jin, R. Zhang, *Experimental and numerical study on chloride transmission in cracked concrete,* Construction and Building Materials 127 (2016) 425-435.

[5] T. Liu, R. Weyers, *Modeling the dynamic corrosion process in chloride contaminated concrete structures,* Cement and Concrete Research 28(3) (1998) 365-379.

[6] J. Xia, T. Li, J.-X. Fang, W.-l. Jin, *Numerical simulation of steel corrosion in chloride contaminated concrete,* Construction and Building Materials 228 (2019) 116745.

[7] X. Cheng, Q. Su, F. Ma, X. Liu, X. Liang, *Investigation on crack propagation of concrete cover induced by non-uniform corrosion of multiple rebars,* Engineering Fracture Mechanics 201 (2018) 366-384.

[8] Z. Cui, A. Alipour, *Concrete cover cracking and service life prediction of reinforced concrete structures in corrosive environments,* Construction and Building Materials 159 (2018) 652-671.

[9] J. Chen, W. Zhang, X. Gu, *Modeling time-dependent circumferential non-uniform corrosion of steel bars in concrete considering corrosion-induced cracking effects,* Engineering Structures 201 (2019) 109766.

[10] X. Zhu, G. Zi, *A 2D mechano-chemical model for the simulation of reinforcement corrosion and concrete damage,* Construction and Building Materials 137 (2017) 330-344.

[11] S. Kranc, A.A. Sagüés, *Detailed modeling of corrosion macrocells on steel reinforcing in concrete,* Corrosion Science 43(7) (2001) 1355-1372.

[12] O.B. Isgor, A.G. Razaqpur, *Modelling steel corrosion in concrete structures,* Materials and Structures 39(3) (2006) 291-302.

[13] C. Cao, M.M. Cheung, B.Y. Chan, *Modelling of interaction between corrosion-induced concrete cover crack and steel corrosion rate,* Corrosion Science 69 (2013) 97-109.

[14] W.-l. Qiu, R.-x. Peng, M. Jiang, *Investigation on the prediction of reinforcement corrosion-induced cover time-vary cracking from multi-scale,* Structures, Elsevier, 2022, pp. 1305-1314.

[15] U.M. Angst, *Predicting the time to corrosion initiation in reinforced concrete structures exposed to chlorides,* Cement and Concrete Research 115 (2019) 559-567.

[16] U. Angst, B. Elsener, C.K. Larsen, Ø. Vennesland, *Critical chloride content in reinforced concrete - A review,* Cement and concrete research 39(12) (2009) 1122-1138.

[17] O. Geng, Y. Yuan, H. Zhu, F. Li, *Experimental study on diffusion coefficient of oxygen in concrete,* Journal of southeast university (Natural science edition) 36 (2006) 191-194.

[18] A. Poursaee, Corrosion of steel in concrete structures, *Corrosion of Steel in Concrete Structures,* Elsevier2016, pp. 19-33.

[19] J. Ožbolt, F. Oršanić, G. Balabanić, M. Kušter, *Modeling damage in concrete caused by*

corrosion of reinforcement: coupled 3D FE model, International journal of fracture 178(1-2) (2012) 233-244.

[20] R. François, S. Laurens, F. Deby, *Corrosion and Its Consequences for Reinforced Concrete Structures,* Elsevier2018.

[21] B. Šavija, M. Luković, J. Pacheco, E. Schlangen, *Cracking of the concrete cover due to reinforcement corrosion: a two-dimensional lattice model study,* Construction and Building Materials 44 (2013) 626-638.

[22] Z. Amalia, D. Qiao, H. Nakamura, T. Miura, Y. Yamamoto, *Development of simulation method of concrete cracking behavior and corrosion products movement due to rebar corrosion,* Construction and Building Materials 190 (2018) 560-572.

[23] D. Qiao, H. Nakamura, Y. Yamamoto, T. Miura, *Crack patterns of concrete with a single rebar subjected to non-uniform and localized corrosion,* Construction and Building Materials 116 (2016) 366-377.

[24] S.Y. Jang, B.S. Kim, B.H. Oh, *Effect of crack width on chloride diffusion coefficients of concrete by steady-state migration tests,* Cement and Concrete Research 41(1) (2011) 9-19.

[25] A. Akhavan, F. Rajabipour, *Quantifying the effects of crack width, tortuosity, and roughness on water permeability of cracked mortars,* Cement and Concrete Research 42(2) (2012) 313-320.

[26] M. Valipour, M. Shekarchi, P. Ghods, *Comparative studies of experimental and numerical techniques in measurement of corrosion rate and time-to-corrosion-initiation of rebar in concrete in marine environments,* Cement and Concrete Composites 48 (2014) 98-107.

[27] M. Shekarchizadeh, M. Valipour, F. Pargar, *Study of Corrosion in Reinforced Concretes with Different Water to Cement Ratios at Splash zone,* (2013).

[28] *ACI 318, Building Code Requirements for Structural Concrete (ACI 318-14): An ACI Standard; Commentary on Building Code Requirements for Structural Concrete (ACI 318R-14),* American Concrete Institute, 2014.